CHEMISTRY

The void formation behaviors in working solid-state Li metal batteries

Yang Lu[1], Chen-Zi Zhao[1,2], Jiang-Kui Hu[3], Shuo Sun[1], Hong Yuan[3], Zhong-Heng Fu[1], Xiang Chen[1], Jia-Qi Huang[3], Minggao Ouyang[2], Qiang Zhang[1]*

The fundamental understanding of the elusive evolution behavior of the buried solid-solid interfaces is the major barrier to exploring solid-state electrochemical devices. Here, we uncover the interfacial void evolution principles in solid-state batteries, build a solid-state void nucleation and growth model, and make an analogy with the bubble formation in liquid phases. In solid-state lithium metal batteries, the lithium stripping–induced interfacial void formation determines the morphological instabilities that result in battery failure. The void-induced contact loss processes are quantified in a phase diagram under wide current densities ranging from 1.0 to 10.0 milliamperes per square centimeter by rational electrochemistry calculations. The in situ–visualized morphological evolutions reveal the microscopic features of void defects under different stripping circumstances. The electrochemical-morphological relationship helps to elucidate the current density– and areal capacity–dependent void nucleation and growth mechanisms, which affords fresh insights on understanding and designing solid-solid interfaces for advanced solid-state batteries.

INTRODUCTION

Solid-state batteries are promising candidates for next-generation batteries, which use highly safe solid-state electrolytes (SSEs) to avoid the potential combustion risk derived from organic liquid electrolytes (1–4). Using Li metal anodes can realize a breakthrough in energy density (5). However, there are various anodic failures in solid-state batteries including severe contact loss and dendrite penetration, especially when operating at a high current density (>3 mA cm^{-2}) with a high areal capacity (>3 mA·hour cm^{-2}) (6). The anodic Li kinetic processes at the solid-solid interfaces dominate the failure of working batteries (7, 8). The basic Li kinetic processes at the Li metal/SSE interfaces include Li-ion transport, interfacial charge transfer, the Li adatom, and vacancy diffusion (9, 10). Because of the extremely low intrinsic diffusion coefficient (<10^{-11} cm^2 s^{-1}) (11–13), the Li stripping–derived Li vacancies cannot be completely replenished and are accumulated as the Li voids neighboring interfaces (14, 15). Therefore, the Li vacancy diffusion is the rate-determining step for dynamic evolution of interfacial morphology (16).

The anodic void accumulation is one of the most notable triggers for the rapid failure of solid-state batteries. The Li void accumulation will gradually degrade the interfacial contacts that lead to the increased local current density and accelerate the subsequent Li plating at solid-solid interfaces until the dendrite failure (17–19). On one hand, the remained contact areas are bearing much-increased local current density because of void formation, resulting in lithium metal accumulation and harmful Li dendrite growth. On the other hand, solid-state Li metal batteries (SSLMBs) are operated at various current densities and capacities in practical situations, which generate various morphological characteristics of Li interfaces (20). Li voids produced in high-rate cycling accumulate rapidly, separating anodes and SSEs and leading to extremely high interfacial impedance ("contact loss" phenomena) (21). Those phenomena are frequent in high current density (>1 mA cm^{-2}) and high-capacity situations (>3 mA·hour cm^{-2}), but the interfacial features and reversibility are unpredictable and uncontrollable yet. The key issue is the elusive interfacial Li void production and evolution mechanism, which require in-depth interpretation. Unraveling the interfacial anodic Li void formation and growth mechanism comprehensively not only can interpret the unknown Li void evolved interfacial failure mechanisms but also supports the related strategy designs in working batteries.

The Li void accumulation induces interfacial morphological evolution. There are few direct and quantitative studies on evolution kinetics at practical current densities and capacities. Some powerful methods such as synchrotron x-ray computed tomography or solid-state nuclear magnetic resonance can help to evaluate the void-induced contact loss and dendrite failures in a nondestructive way (22–27). Considering the buried Li/SSE interfaces, the observations still confront dilemmas (28), where the resolution is insufficient to unravel the key morphological features of voids. While the electrochemical impedance spectra (EIS) help to quantify the contact loss with the increased charge transfer impedance of the Li/SSE interface (29). The impedance is in reverse ratio with the active area (10, 30). The void accumulations can also be demonstrated by density functional theory (DFT) calculations (31), molecular dynamics simulations, and kinetic Monte Carlo simulations (32, 33). Consequently, on one hand, the void formation and accumulation processes should be quantified at different electrochemistry conditions to imitate various application scenarios. On the other hand, high-resolution observations toward microscopic morphological features under different stripping circumstances are also essential to building a direct connection between electrochemistry and morphological evolution. To provide a comprehensive understanding, the Li void evolution should be observed and quantitatively analyzed in multiple scales.

In this contribution, we elucidated the interfacial Li void formation and evolution mechanism in solid-state batteries by multiscale observations and quantifications. We draw an analogy between Li void behaviors and the bubble production processes in liquid phases to understand the Li void formation and growth mechanisms (Fig. 1).

[1]Beijing Key Laboratory of Green Chemical Reaction Engineering and Technology, Department of Chemical Engineering, Tsinghua University, Beijing 100084, China. [2]State Key Laboratory of Automotive Safety and Energy, School of Vehicle and Mobility, Tsinghua University, Beijing 100084, China. [3]Advanced Research Institute of Multidisciplinary Science, Beijing Institute of Technology, Beijing 100081, China.
*Corresponding author. Email: zhang-qiang@mails.tsinghua.edu.cn

Considering the nucleation and growth theory, if we treat the bulk Li metal as a "solution," then the voids can be seen as "bubbles" in it. After the voids are formed at the interfaces due to the Li stripping, the voids will diffuse into the bulk Li because of the intrinsic void diffusion, which is just like the "bubble floating." The diffusion coefficient can be regarded as "floating rate." Under the high current density, the "void bubbles" will be formed rapidly. Because the floating rate of the bubbles is fixed, the void bubbles will accumulate at the interfaces. The Li void formation phenomena are unraveled by macroscopic electrochemistry quantifications, multiscale microscopic observations, and atomic DFT analyses. At macroscopic view, the in situ galvanostatic electrochemical impedance spectroscopy (GEIS) and the distribution of relaxation time (DRT) are applied to quantify the interfacial contact loss process induced by different current densities and capacities. The microscopic morphological feature and evolution processes are observed by plasma focused ion beam–equipped scanning electron microscope (PFIB-SEM) and operando optical observations. Combining with nucleation and growth theory, the void nucleation size and distribution density are determined by current density, and the void growth exhibits a zero-dimensional (0D) to 3D evolution driven by the atomic energy increase after stripping forming regular porous size. The void formation kinetics are highly dependent on the current densities and capacities. Regulating the void nucleation and growth plays a vital role in stabilizing the interfaces of SSLMBs in different application scenarios.

RESULTS

The interfacial contact loss of Li/SSE is recorded by operando GEIS in a Li-Li$_7$P$_3$S$_{11}$-In half cell. Li-In works as the counter and the reference electrode to distinguish the single Li stripping kinetics. Because of the stable lithiation potential and low charge transfer impedance of Li-In alloys, the battery degradation of polarization and internal impedance can be mainly attributed to the stripped Li/SSE interfaces. The single Li stripping processes can be distinguished by evaluating the Li-Li$_7$P$_3$S$_{11}$-In half cells.

Quantification on the contact loss

The total impedance evolutions and quantification of the Li-Li$_7$P$_3$S$_{11}$-In half cells are displayed in Fig. 2. The exhibited GEIS is evaluated from 1 to 10 mA cm^{-2}, and the related impedances are measured with a capacity interval of 0.5 mA cm^{-2}. The GEIS measured at the current density of 1, 2, 5, and 10 mA cm^{-2} is displayed in Fig. 2 (A to D), respectively. The voltage-time and voltage-capacity curves evaluated at different current densities are displayed in fig. S1. These half cells will fail once the open circuit exhibits a voltage of <−1.0 V versus Li/Li$^+$.
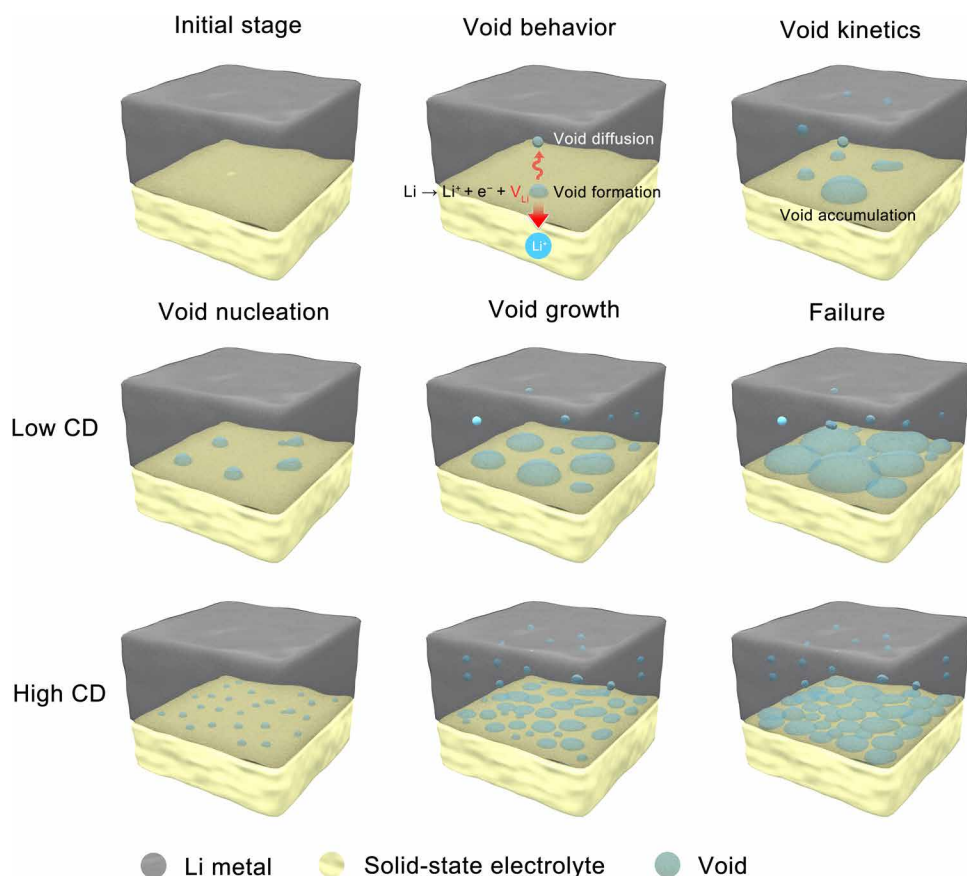

Fig. 1. Schematic shows the interfacial Li void behaviors and Li void nucleation and growth phenomena. Li voids form during Li stripping processes. The diffusion of the Li voids can retard the void accumulations. The Li void kinetics at the interface and Li metal can be demonstrated as bubbles in the "liquids." Different current densities (CD) will lead to various void formation processes. Low current density will lead to large critical void nuclei and slow void growth with highly effective areal stripping capacities. High current density induces more void nucleuses sites with small sizes. The voids grow fast, resulting in rapid contact loss in the porous Li metal.

There is a continuous increase of impedance during the Li stripping. The initial impedances remain stable at ~80 ohms for all samples. The impedance can remain less than 150 ohms until 5.0 mA·hour cm^{-2} at 1.0 mA cm^{-2} (Fig. 2A). The subsequent impedance will markedly increase to hundreds of ohms (fig. S2). The "effective capacity" is the total stripping capacity during the stripping test until the cutoff voltage (−2 V). The effective capacities for Li stripping at increased capacity will reduce from 4.0, 3.0, to 2.0 mA·hour cm^{-2} at the current density of 2.0, 5.0, and 10.0 mA cm^{-2}, respectively (Fig. 2, B to D). The impedance increasing rates also exhibit discrepancy with increased current density. The impedance of this battery is composed of the intrinsic ohm impedance, the SSE grain boundary impedance (R_{GB}), the Li/SSE interfacial impedance ($R_{Li/SSE}$), the possible solid-state interphase impedance (R_{SEI}), and the indium-involved lithiation kinetics impedance (R_{Li-In}), which is displayed in fig. S3A. The battery-involved R_{GB}, R_{In}, and $R_{Li/SSE}$ simultaneously depended on

the active area. The DRT technique is involved in profound analyses of the EIS profiles in this contribution.

The DRT of the GEIS results (Fig. 2, A to D) are displayed in Fig. 2 (E to H), respectively. Each relaxation time τ in the DRT plot represents the specific electrochemical process (34, 35). The impedance can be separated from a single peak at $\tau = 10^{-6}$ s, which represents the grain boundary response (36). The τ from 10^{-4} to 1 s demonstrates the kinetics of the Li metal and the In lithiation (fig. S3B). It is hard to distribute the kinetic discrepancy with a low stripped Li content (<2 mA·hour cm^{-2}). However, the grain boundary impedances of SSEs (R_{GB}, $\tau = 10^{-6}$ s) deliver continuous evolutions with the rise of Li stripping. Meanwhile, all DRT peaks increase simultaneously at the end of the Li stripping stages (increased intensity in the contours). In contrast, the Li stripping in Li-In symmetric cells exhibits another character on impedance evolution. The impedance at high frequency (10^6 to 10^5 Hz) still remains stable with a high Li stripping
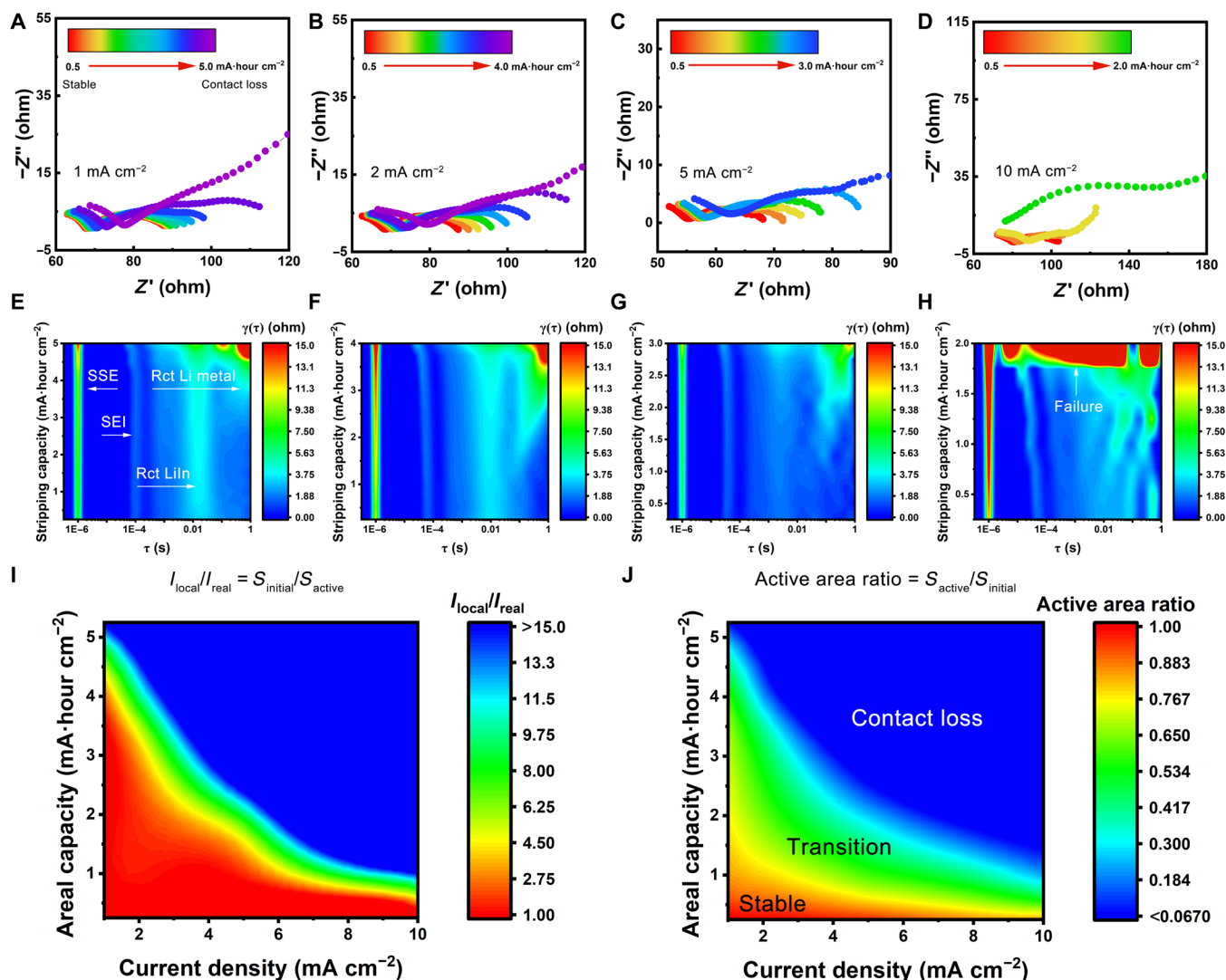

Fig. 2. GEIS evaluation for Li half batteries during Li stripping process. The EIS recorded at the current density of (**A**) 1 mA cm^{-2}, (**B**) 2 mA cm^{-2}, (**C**) 5 mA cm^{-2}, and (**D**) 10 mA cm^{-2} and (**E** to **H**) corresponding DRT transition result of (A) to (D), respectively. The color evolution in the legends of (A) to (D) from red to purple represents the increased stripping capacity from low to high during the EIS measurement. Rct, charge transfer impedence. The quantified contour type of areal capacity–current density contact loss phase diagram is exhibited at (**I**) local current density view and (**J**) active contact area view.

capacity (>5 mA·hour cm^{-2}; fig. S4), and the corresponding DRT peak at 10^{-6} s remains stable. The alloy can maintain the interfacial contacts, avoiding the contact loss derived from the void accumulation. Considering the basic equation of $R = \frac{\rho L}{S}$ (where ρ is resistivity, L is length, and S is area), those phenomena demonstrate that a Li stripping–induced factor will lead to the proportional rise on the total impedance, which is attributed to the reduced anodic active area. It is concluded that the R_{GB} can be separated and is independent on the dynamic electrochemical processes, which is appropriate to interpret the anodic contact loss.

The Li stripping will result in anodic contact loss. Li metal works as a current collector at a single side. Hence, the total impedance of a half cell will be determined by the contact loss. A simple equivalent calculation helps to quantify the contact loss (fig. S5). Here, the initial active area is the circle with a diameter of b, and the active area after Li stripping is equivalent to an imaginary circle with a diameter of a (fig. S6). The SSE impedance can be separated from the total impedance. As calculated, the SSE impedance after Li stripping (R_{strip}) is $\frac{\rho L}{\pi ab}$. The mathematic deduction process for the impedance is provided in the Supplementary Materials. Hence, the local current density ratio after Li stripping is defined as $\frac{I_{local}}{I_{real}} = \frac{S_{initial}}{S_{active}} = \left(\frac{R_{active}}{R_{initial}}\right)^2$, which quantifies the contact loss. Here, we quantified the R_{GB} evolution in continuous Li stripping at a current density of 1 to 10 mA cm^{-2} and drew the contour phase diagrams (Fig. 2I) with parameters of current density, capacity, and the local current density ratio. The EIS quantified by DRT exhibits similar accuracy compared with conventional evaluation (fig. S7). The intensity color distinguishes the interfacial stability of red as a stable region with a small local current density ratio of less than 2.75, transition region with color from orange to light blue delivering the ratio from 3 to 12, and the blue region of failure with a ratio of more than 15. The residual active contact area ratio is defined as $\frac{S_{active}}{S_{initial}}$. This area ratio can directly exhibit the contact loss phenomena. Hence, the relationship among current density, stripped capacity, and the active area ratio is visualized in Fig. 2J. The red region is the stable region with an active area of $>80\%$. The active contact degradation from 70 to 30% presents the transition from stable stripping to contact loss failure.

Multiscale observation toward contact loss

The phase diagram in Fig. 2J displays the contact loss from a macroscopic view. Briefly, the macroscopic phenomena are accumulated from the microscopic evolutions. The phase diagram exhibits three dimensions demonstrating the contact loss including the current density, the capacity, and the transition boundary. These are key factors unraveled by the phase diagram and deliver specific microscopic characters, which can analyze the Li stripping kinetics mechanism. The Li stripping–induced morphological evolution is multiscale monitored (Fig. 3). The stripping current densities are 0.5 mA cm^{-2} for operando optical observations and 1 mA cm^{-2} for ex situ observation by PFIB-SEM. The operando optical method provides the contact loss evolution at a length scale of hundreds of micrometers. However, the observation area of operando optical facilities is restricted on the outside boundary. The internal morphological features cannot be acquired in a detailed length scale. The PFIB-SEM can realize a high-resolution observation for the internal buried interfaces by cutting a smooth interfacial cross section. The PFIB-SEM uses the inert Xe$^+$ as milling source, which can significantly increase the milling efficiency and avoid strong radiation damage of Li metal (*37, 38*), which can acquire smooth morphology after milling at room temperature as that milled by cryo-FIB (fig. S8) (*39*).

The operando optical observation describes the contact loss phenomena at the submacroscopic scale. The schematic of the optical observation is displayed in Fig. 3A. The outside boundary is the restricted area for observations. The triple layers of Li metal foils, SSEs, and current collectors can be detected. At the initial discharge stages, no obvious change can be observed (0 to 0.67 mA·hour cm^{-2}/ initial to 80 min of Li stripping). After continuous Li stripping for 0.83 to 1.17 mA·hour cm^{-2}/100 to 140 min, the point defects exhibit an obvious extension (arrow), and some continuous voids are also enlarged with increased point defects (dashed circle). The interface exhibits a gradual overall separation at the final stages of 1.33 to 1.67 mA·hour cm^{-2}/160 to 200 min (dashed line).

The detailed void morphology features are observed by PFIB-SEM samples in standard model cells. The schematic illustration of the PFIB-SEM method for evaluating the void morphology is displayed in Fig. 3B. Li-In alloy as a counter electrode has a stable potential (0.62 V versus Li/Li$^+$) for continuous lithiation. The polarization changes can be attributed to the kinetics of Li metal stripping. The relationship between void evolution and discharge curve for Li stripping is displayed in Fig. 3C. The initial interfacial status before Li stripping exhibits intimate contact. Almost no void or defect can be found. Once the Li stripping starts, 0D small defects (1 to 2 μm) will emerge with a Li stripped capacity of 1.0 mA·hour cm^{-2}, where the major interfacial contacts still remain. Then, defects exhibit a 2D extension with a rising capacity to 2.0 mA·hour cm^{-2}. The polarization remains stable as a flat plateau. It proves that the defects incline to be initially formed at areas adjoined interfaces. Subsequently, a 3D development for the interfacial voids is detected (3.0 mA·hour cm^{-2}). The interfacial defects are completely interconnected and widened as obvious cracks. The residual interfacial Li is inclined to pulverize. The polarization has exhibited a declined tendency (-0.05 V versus Li/Li$^+$). Last, the Li metal and the SSEs are almost separated at a capacity of 4 mA·hour cm^{-2}. The polarization shows the synchronous increase (-0.10 V versus Li/Li$^+$). The increased polarization is consistent with the impedance results. The void accumulation delivers a basic development principle of the emerging 0D defects, the 2D extension of defects, the interconnection of the 2D defects, and the final 3D expansion–induced complete contact loss.

The plane distribution of vacancies is demonstrated in Fig. 4. Virtually, after fully Li stripping, the residual interfacial Li metal has proved the inhomogeneous Li stripping (fig. S9). To exhibit the plane overview of the distribution of interfacial defects, the time-of-flight secondary ion mass spectrometry (TOF-SIMS) is used to unravel the interfacial characteristics from the top view. Figure 4A illustrates the measurement process, in which each frame for TOF-SIMS sampling will strip a layer of lithium and will be collected by the SIMS receiver. It can reflect the Li distribution, get rid of the upward dense lithium, and expose and capture the interfacial defects cooperating with SEM. The sampling process can also help to expose the Li morphology adjoining the interfaces underneath. The total sampling intensity can distinguish the dense Li and the voids (fig. S10). As displayed in Fig. 4B, compared with the SEM image (fig. S11), the TOF-SIMS for bulk Li exhibits the overview element distribution of the Li from the top view and the side view. The P and S signal of Fig. 4B is displayed in fig. S12. The color bar shows the intensity of the Li signal in the figures. The red area indicates a high relative Li signal intensity, which represents the existence of Li metal. The yellow or green area represents the reduced Li signal intensity, representing the porous Li with voids. The blue represents the low
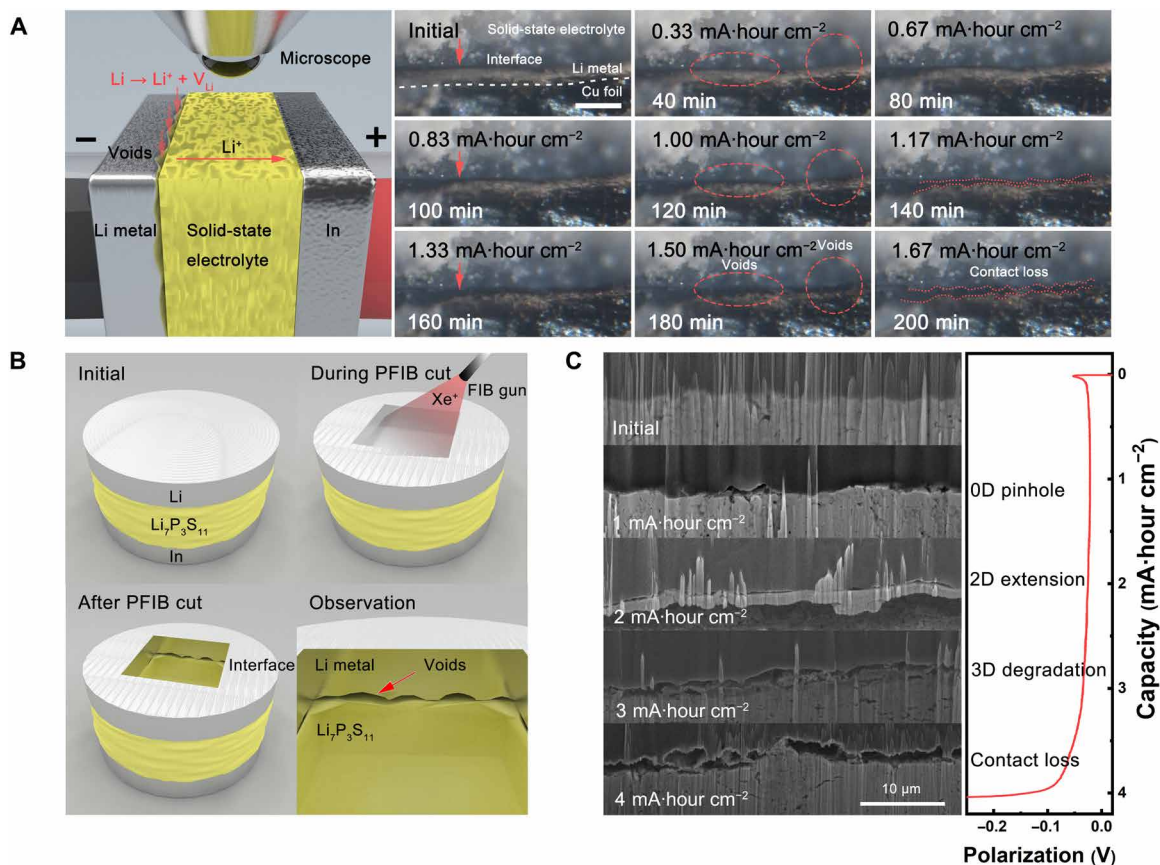
Fig. 3. Multiscale observations toward interfacial Li voids during Li stripping. (**A**) Operando optical observations for Li/SSE interfaces during continuous Li stripping at a current density of 0.5 mA cm^{-2}. Scale bar, 50 μm. (**B**) The schematic of the ex situ FIB-SEM method for detecting the interfacial evolution after Li stripping. (**C**) The polarization curve of Li-Li$_7$P$_3$S$_{11}$-In half cell, where the interfacial morphological evolution during continuous Li stripping is measured at 1 mA cm^{-2}. The polarization decrease during Li stripping validates the interfacial Li depletion.

relative Li signal intensity, which presents the voids or the absence of Li metal. The upward dense Li exhibits strong intensity. The in-depth view of the weak Li intensity indicates Li depletion/void accumulation at the working interfaces. Then, the inner morphologies underneath dense Li are unraveled by TOF-SIMS with different frames. The influence of possible radiation damage toward Li morphology during TOF-SIMS evaluation can be neglected when the beam current is less than 1 nA (fig. S13). After continuous TOF-SIMS sampling, the upward dense Li has obviously been removed, and the porous morphologies are gradually exposed (TOF-SIMS stripped for 150 to 300 frames), proving the porous and pulverized morphology distribution after continuous Li discharge (Fig. 4C), which exhibit similar morphology characteristics at a cross-sectional view.

Current density induced Li voids

Different defect characters are highly dependent on the applied current densities. The defects are evaluated from three views. The first view is derived from the cross section of a fixed stripping capacity of 2.0 mA·hour cm^{-2} with different current densities (1 to 10 mA cm^{-2}; Fig. 5A). The cross sections are captured by PFIB-SEM. The low current density (1 mA cm^{-2}) is inclined to form a concentrated defect of nearly 10 μm, which can be foreseen from the void growth from a single nucleus. The dispersed defects with smaller sizes can be achieved with the rise of current densities, which can be estimated

from the growth of multiple void nuclei. The capacity of 2 mA cm^{-2} will form a mixed defects style of a concentrated point defect (2 to 3 μm) and extended defects. The defect size in 5 mA cm^{-2} will be subsequently reduced from ~400 nm to 1 μm. The extremely high current density of 10 mA cm^{-2} will directly result in fine microscopic pores in working Li metal anodes.

The second view is the Li stripping depletion morphologies, which are also measured at 1 to 10 mA cm^{-2} (Fig. 5B). The low current density (1 mA cm^{-2}) induces continuous contact loss. The porous contact loss depletion morphology is observed when a large current density is applied. The porous size will shrink with the rise of current densities. The morphology degradation is exacerbated into tiny pores with a size of <500 nm at a depletion of 10 mA cm^{-2}. The third view is the top view of residual Li on the SSEs after Li stripping depletion (Fig. 5C), which can directly reflect the real status of the contact loss depletion, contributing to demonstrating the Li void growth processes. The residual Li will be automatically separated to observe the surface of Li metal; clear "holes" remain on the Li metal surface (fig. S14). The Li stripping depletion can be demonstrated by the morphological features of the holes on the Li metal with different current densities (1 to 10 mA cm^{-2}; Fig. 5C). The hole can magically form a pentagon or hexagon porous network. The average sizes (r) of Li stripping depletion holes gradually reduced from 4.1, 2.4, 0.9, and 0.4 μm with current densities of 1, 2, 5, and 10 mA cm^{-2}, respectively. The
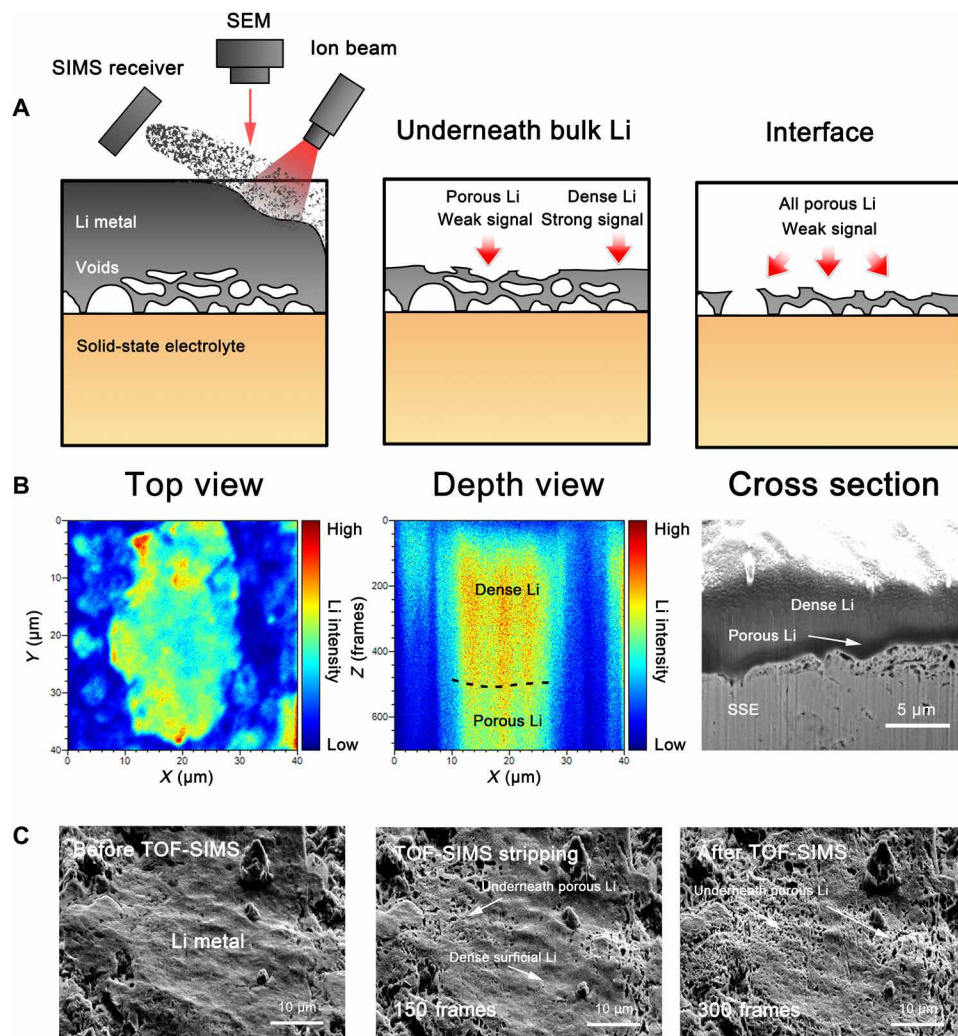
Fig. 4. The TOF-SIMS analysis from the bulk Li metal to the interfaces. (**A**) Schematic shows the mechanism toward TOF-SIMS method on analyzing the Li metal on the interfaces. (**B**) The top and depth view on Li intensity distribution of Li metal by complete TOF-SIMS imaging compared with the SEM cross-sectional images. The color bars from red to blue of the TOF-SIMS images represent the Li intensity from high to low. (**C**) The morphology evolution of Li after 150 and 300 frames by TOF-SIMS Li stripping, which displays the morphological features from the bulk to the interfaces.

homogenous size distributions of the void frameworks are further validated by SEM images (fig. S15). The interpretation toward the formation process of the regular Li framework can support the void growth mechanism. Although the Li depletion voids exhibit the shape of pentagons or hexagons, the Li depletion morphology is not related to the intrinsic Li grain size. As evaluated by electron back-scattered diffraction (EBSD), the Li metal grain sizes are estimated as >100 μm (fig. S16), which exhibit obvious discrepancy with those of the Li voids (<10 μm). The Li networks are detected in the failed Li metal. Hence, the sizes of the networks are called critical sizes, which are the smaller unit of failure Li voids after stripping.

DISCUSSION
Void nucleation and growth mechanism
The Li void framework morphology can be interpreted by nucleation and growth theory. Briefly, the void size and their distributions are depended on the applied current density. Low current density results

in few void nuclei with large sizes, high current density renders more void nuclei with small sizes, and then the void nuclei with different sizes will grow up into "void grains" (Fig. 5D). The detailed mechanisms are further inferred below.

Stage I void nucleation
The microscopic evolution is attributed to the energy evolution of interfacial Li atoms after Li stripping. The out-of-balance flux leads to the void appearance. If we treat lithium as a "solvent," then the fresh voids can be seen as a "deposited fresh phase" (*40*). The nucleation theory is further extended to describe void accumulation processes. The driven force for the void nucleation also derives from the interfacial overpotential (η). Consequently, the nucleation barrier (ΔG_v) relationship between current density (*i*), area-specific impedance (R_s), and the critical radius of the voids nucleus (r_{crit}) can be expressed as Eq. 1 (*41–43*)

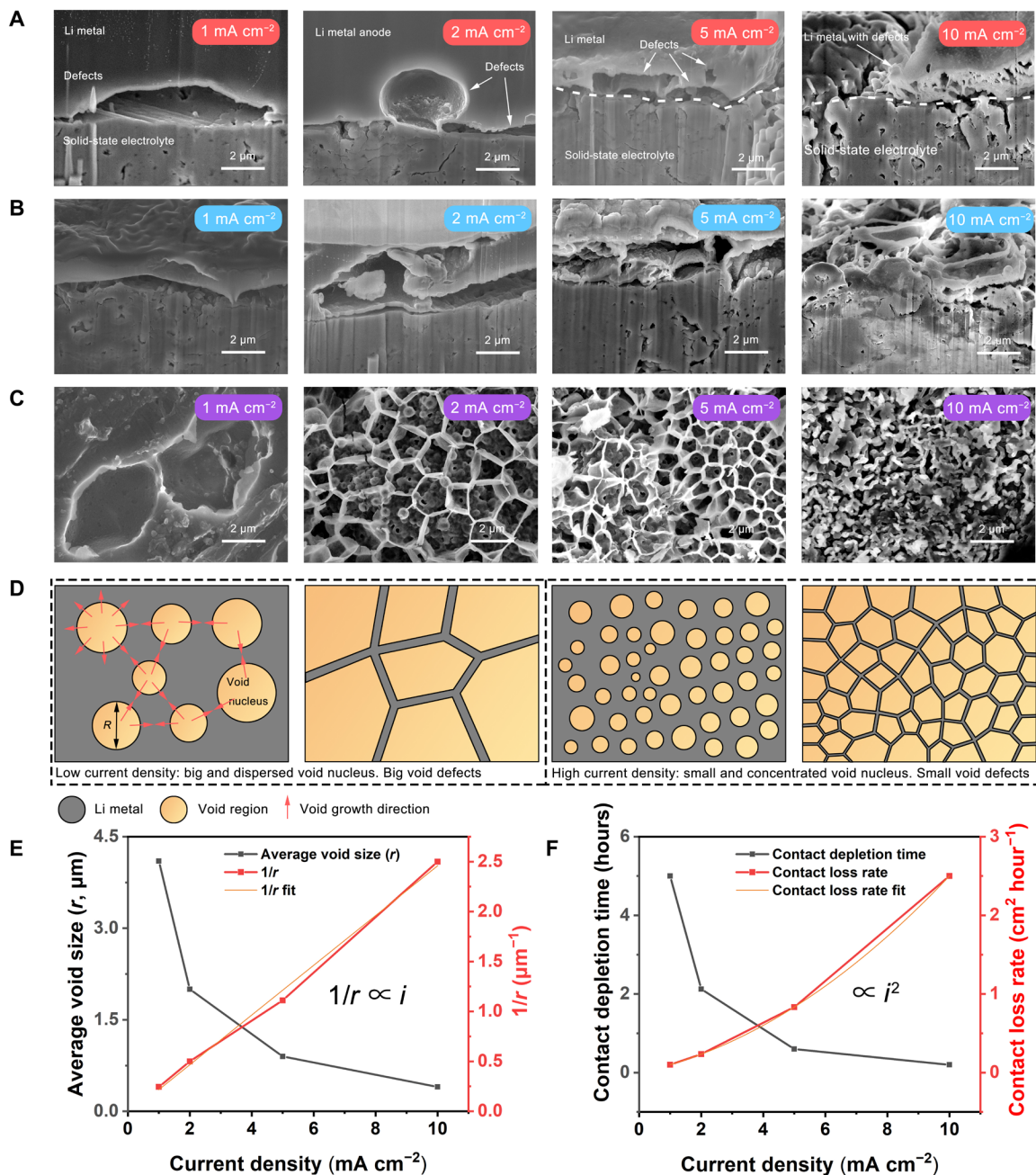$$\Delta G_v = -\frac{F\eta}{V_m} = -\frac{FiR_s}{V_m} \qquad (1)$$

Fig. 5. The microscopic characters and quantification relationship of interfacial defects. (**A**) The cross section of the defects formed at a fixed capacity of 2 mA·hour cm^{-2} with a current density of 1 to 10 mA cm^{-2}. (**B**) The cross section of the contact loss failure derived from the Li stripping depletion. (**C**) The morphology of residual Li at the top view after the complete Li stripping. (**D**) The schematic shows the void formation process at the top view with low and high current density. (**E**) The relationship between average void sizes and the current density. (**F**) The relationship among contact depletion time, contact loss rate, and the adopted current density.

$$r_{\text{crit}} = \left| \frac{2\gamma_{\text{Li}}}{\Delta G_v} \right| \propto \frac{1}{i} \qquad (2)$$

where F is the Faraday constant. V_m means the molar volume of lithium metal. γ_{Li} is the specific surface energy of lithium metal. It is seen that the contact area (area-specific impedance) also controls the interfacial Li kinetics.

Hence, it is concluded that the critical radius of the Li void nucleus is in the reverse ratio of applied current densities (Eq. 2), which is consistent with our experimental evaluations of the linear relationship

between $1/r$ and the current densities (Fig. 5E). The typical void nucleus is displayed in fig. S17, which is difficult to capture for direct observations at the initial stages.

Stage II void growth

The void growth process includes two processes: void nucleation and void growth. The new voids nucleate at the initial stage, and the formed new vacancies attach to the void nuclei exhibiting the growth process.

The void growth rate V_{void} can also be written as Eq. 3 (44). The detailed deduction is provided in the Supplementary Materials

$$V_{void} = \nu\, n_{new\ voids}\, S_{nucleus} \tag{3}$$

$$\nu = \nu_0 \exp\left(-\frac{\Delta G_m}{RT}\right) \tag{4}$$

$$n_{new\ voids} \propto J_v - J \approx \frac{i}{F} \tag{5}$$

$$S_{nucleus} \propto i \tag{6}$$

where the $n_{new\ voids}$ represents the number of new voids derived from the Li stripping and the $S_{nucleus}$ represents the specific surface area of nuclei (Eq. 3). ν represents the collision frequency among the new voids with the void nuclei, and ΔG_m represents the migration energy of the vacancies (Eq. 4). R and T mean the ideal gas constant and temperature, respectively. J_v means the Li void flux derived from current loading, and J means the intrinsic void diffusion flux. i is the current loading, and F is the Faraday constant (Eq. 5).

Hence, the growth rate is in proportion to i^2 at the same temperature. The new voids are determined by current density i as shown in Eq. 5, and the total specific surface area of the void nucleus is also proportional to the current density i (Eq. 6 and Supplementary Materials). The detailed deduction is provided in the Supplementary Materials. The theoretical conclusion is consistent with our experimental result evaluated by calculating the depletion time during the Li stripping (Fig. 5F).

Stage III failure
The interfacial Li cannot replenish the void accumulation at the final stripping stage. The growth direction of the void will be extended from horizontal growth along with the interface (XY axis, 2D growth) to vertical growth (Z axis, 3D growth).

During the void growth stage, it is inclined to follow the linear growth along with the interfaces due to the location position. The line growth rate $\left(\frac{dr}{dt}\right)$ can be written as Eq. 7

$$\frac{dr}{dt} = \alpha\nu \exp\left(-\frac{\Delta G_a + \Delta g}{k_B T}\right) = \alpha\nu \exp\left(-\frac{-\frac{F i R_s}{V_m} + l \cdot \Delta g_l}{k_B T}\right) \tag{7}$$

where α is the amount of the void per area, ΔG_a is the driven force for void formation, Δg is the void migration barrier from other sites, l is the void migration distance, Δg_l is the migration barrier per unit distance, and ν is the vibration frequency. Hence, the 2D extension dominates the total growth of the void along with the interface at this stage. The high current density will result in the void collision probability, which reflects in a porous structure.

Considering the advantages of Li^0 surficial diffusion (4×10^{-7} cm^2 s^{-1}) over the bulk vacancy diffusion (10^{-11} cm^2 s^{-1}) (45), the vertical growth of voids is completely derived from the intrinsic adatom replenishment. The growth rate is directly related to the adatom energy. Therefore, we construct the Li/Li$_2$S model to evaluate the energy change of the interfacial atomic energy after the injection of the voids. As displayed in Fig. 6A, the interfacial Li atomic energy is basically homogeneous before the void injection. If a void is injected into the interface, then the Li atomic energy begins to fluctuate. With the continuous void injection, on one hand, the atom will concentrate at the defect area. On the other hand, the interfacial energy of these

atoms is increased, and with the accumulation of the voids, the atomic energy will be continuously increased (ΔE), demonstrating the elevated migration tendency of the high-energy atoms. Hence, the vertical growth rate of the voids can be written as Eq. 8

$$V_{vertical} = \alpha\nu \exp\left(-\frac{\Delta g - \Delta E}{k_B T}\right) \tag{8}$$

With the accumulation of the voids, the tendencies of total atomic surficial energies remain increasing. Hence, the vertical growth rate will be continuously increased. This can interpret the growth of Li voids evaluated from the 2D horizontal growth to the subsequent 3D growth. The 3D growth demonstrates the insufficient replenishment of interfacial Li due to the contact loss, which leads to repaid contact loss failure.

Principles of void accumulations
The electrochemical evaluation proves that the Li void accumulation exhibits three major stages of stable Li stripping, the stable region (red), the transition region (yellow), and the failure region (blue) (Fig. 6B). The microscopic evolution features are also combined in this quantified current density–areal stripping capacity-active contact ratio phase diagram. The current density determines the void accumulation rate, and the capacity determines the level of void accumulations. The void accumulation processes are summarized in Fig. 6C. The void nucleates during the Li stripping with a critical size by $1/i$. The void growth is based on the void nucleus size and amount exhibiting the accumulation rate in proportion to i^2. The void inclines to loss adjoin to the interface to the transition process. Then, the 3D growth is relied on the surficial atomic diffusion because of the atomic energy increase before the failure of contacts. At high current density scenarios, high current density leads to a small nucleus with a high amount, which results in rapid void growth. The high concentration vacancy injection will also lead to a high vacancy collision, exhibiting the porous morphology. The contact loss failure during high current density displays porous contact loss derived from the high amount of nuclei.

We also compare the void behavior in the SSE system and liquid electrolyte system. The detailed discussion of the void features in the liquid electrolyte system is provided in the Supplementary Materials (figs. S18 and S19). The basic void formation behaviors of Li metal are similar in both solid-state batteries and liquid electrolyte batteries, which is proved by the similar relationship between the void sizes and the current density. However, the intrinsic discrepancies are shown in the Li void growth processes (fig. S20). The voids on the solid-solid interfaces block the mass transport, leading to void growth and rapid battery failure. In contrast, the flowing liquid electrolytes guarantee mass transport, inducing new void nucleation on the fresh solid-liquid interfaces.

The pressure-induced influences
If the creep (σ_{creep}) is adopted in the system, then the relationship is written as Eq. 9

$$\Delta G_v = -\frac{F\eta}{V_m} + \sigma_{creep} \tag{9}$$

where F is the Faraday constant ($F = 96,500$ C mol^{-1}) and V_m is the molar volume of lithium metal (1.3×10^{-5} m^3 mol^{-1}).

In general, the external pressure can reduce the $|\Delta G_v|$, and the function of creep can be treated as the reduction of current density.
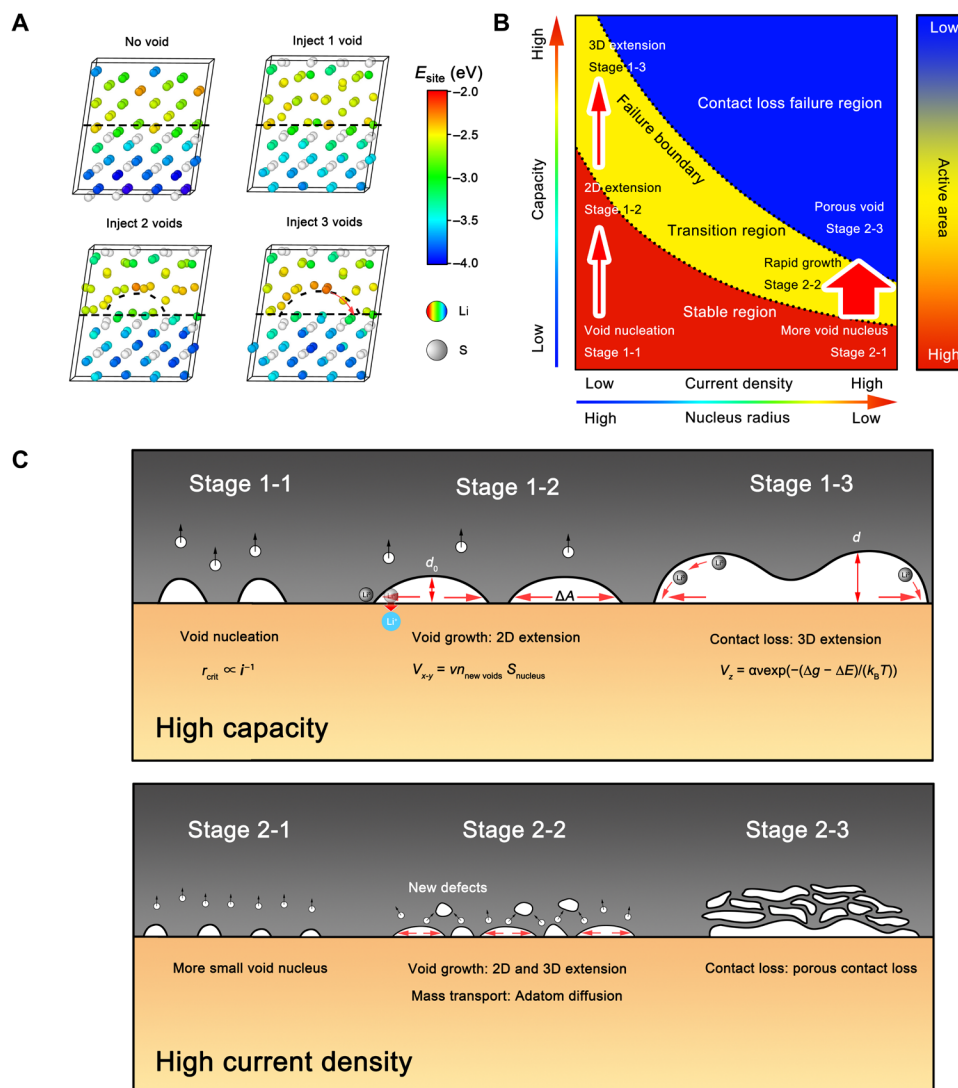
Fig. 6. The interfacial evolution principle during Li stripping and the actual condition of morphology evolution. (**A**) The site energy evolution after void injection by DFT calculations. (**B**) The phase diagram describes the void evolution regulated by the current-stripping areal capacity and current density. (**C**) The schematic of microscopic evolution in different void accumulation circumstances.

γ_{Li} is the specific surface energy of lithium metal. Hence, the critical size (r_{crit}) of the void will increase (Eq. 10), and the amounts of the nucleus will be reduced

$$r_{crit}\uparrow = \left| \frac{2\gamma_{Li}}{\Delta G_v \downarrow} \right| \propto \frac{1}{i\downarrow} \qquad (10)$$

In our case, as the measured interfacial impedance (R_s) is 10 ohms cm^2, the overpotential η is calculated as $J \times R_s = 1 \sim 10$ mA cm$^{-2} \times 10$ ohms cm$^2 = 10$ to 100 mV. Therefore, $-\frac{F\eta}{V_m}$ ranges from 74.2 to 742.0 J m^{-3}, resulting in the required σ_{creep} from 74.2 to 742.0 MPa at the current density of 1 to 10 mA cm^{-2}.

However, the exact stack pressure in our mold cell is around 5 MPa, which can only suppress the void formation at the current density of <0.07 mA cm^{-2}. A previous report also demonstrated that the pressure of >20 MPa will lead to the collapse of electrolytes and the subsequent extrusion of Li metal in sulfide electrolyte–based solid-state batteries (46). Hence, simply applying stack pressure in

sulfide solid-state batteries would not completely eliminate the void nucleation.

According to the modified equation involving creep (Eq. 11), the pressure-induced creep will reduce the activation energy. Hence, the void growth can be regulated by introducing external stack pressures

$$\frac{dr}{dt}\downarrow = \alpha v \exp\left(-\frac{\Delta G_a + \Delta g + \sigma_{creep}}{k_B T}\right)\downarrow \qquad (11)$$

In summary, we discuss the specific effect of pressure-induced creep on both nucleation view and growth view. The equations adequately demonstrate the significance of pressure on suppressing the void nucleation and growth and are also promising to provide quantified guidance on applying proper pressure.

Solutions from void formation theory

The void formation has the nucleation and growth process. Strategies for constraining contact loss can be designed by suppressing

void nucleation and growth. Initially, the existence of void nucleation is due to the limitation of void diffusivity in Li metal. Adopting pressure can increase the void diffusivity, alleviating the void formation. However, the pressure abuse can induce direct overcreep and subsequent dendrite penetration. Developing the intrinsic void diffusivity for Li metal involves atomic design. Altering the crystal structure is the essential route to developing the diffusion. Until now, using and regulating Li alloy components with improved diffusivity are promising strategies (12, 47). Increasing the intrinsic diffusivity (>Li void diffusivity in bulk Li) is the first principle.

Second, in the void nucleation view, according to Eqs. 1 and 2, void nucleation is mainly driven by the interfacial overpotential. Suppressing the interfacial overpotential can suppress the void nucleation. The interfacial overpotential is mainly derived from the interfacial impedance, including the charge transfer impedance and SEI-based impedance. Reducing the interfacial impedance such as improving the initial contact and reducing the interfacial reaction are efficient to alleviate the subsequent contact loss. It is unraveled that the interfacial impedance is not only highly related to the dendrite formation but also plays a key role in inducing the void accumulations. Reducing the interfacial impedance is the second principle.

Third, in the void growth view, according to the evolution phase diagram in Figs. 2J and 6B, the key stage of the void-induced failure is the transition stage, which corresponds to the 2D growth process. Adopting frameworks for Li metal composites is essential to suppress the subsequent growth, which helps to maintain the interfacial contact. It is known that the 2D growth stage is the transition stage from stable contact to failure. The design of the Li framework should consider the critical void size to prevent the 2D void growth before the failure. Hence, the pore size of the framework must be smaller than the void critical size. The critical void size is highly related to the current loading. The critical size is in reverse proportion to the adopted current density. The critical sizes of the Li void provide the references for the design principle of the Li framework. According to the results in Fig. 5C, for instance, the critical size under 10 mA cm^{-2} reaches 0.4 μm. Therefore, if the Li framework composites will operate at 10 mA cm^{-2}, then the framework design must be with a pore size of <0.4 μm to prevent 2D void growth until the critical size. Hence, the Li framework design principle includes comprehensively considering the application current loading of solid-state battery. Constructing frameworks with porosity of lower than critical void size is the third principle.

Fourth, adopting proper external conditions such as pressures can suppress the void growth. The added pressure can be estimated by the "strain rate" theory provided by Sakamoto's group (15). The Li stripping flux derived from current density will lead to the change of the Li metal thickness, which is analogous to a current-induced strain rate. The external pressure will also induce a strain rate. The comparison between the strain rate induced by corresponding pressure and current density is an effective standard. The current density–induced strain rate is given as (15)

$$\varepsilon_j = \frac{JM}{\rho F I_0} \qquad (12)$$

where ε_j is the current-induced strain rate, I_0 is the length, J is the current density, M is the molar mass of Li, ρ is the density of Li, and F is the Faraday constant.

The pressure-induced strain rate is given as (48, 49)

$$\varepsilon_{\text{creep}} = A\sigma^m \exp\left(-\frac{Q}{RT}\right) \qquad (13)$$

where $\varepsilon_{\text{creep}}$ is the strain rate induced by pressure, A is the pre-exponential factor determined by material properties, σ is the stress, m is the power-law creep exponent, Q is the activation energy, R is the molar gas content, and T is the temperature.

Hence, if we control the pressure to realize the $\varepsilon_{\text{creep}} > \varepsilon_j$, then the void formation can be suppressed at the macroscopic view, and the rational pressure can be calculated according to Eqs. 12 and 13. However, it arouses the mechanical failure concern if applying an excessively high pressure, exceeding the yield strength to suppress voids at an extremely high current density (46).

Summary

The Li void formation is one of the most significant origins of battery failure in solid-state batteries. This contribution unravels the interfacial void evolution principles in solid-solid interfaces and illustrates the contact loss phenomena under a variety of current densities (1.0 to 10.0 mA cm^{-2}) by connecting the electrochemical performances with the microscopic morphology. The current densities control the void nucleation, and the capacities control the growth until the contact loss failure. The size of the void nucleus is in reverse proportion to current density and induces the specific area in direct proportion to current density. The total contact loss rate is estimated in proportion to i^2. At microscopic view, the typical contact loss experiences the evolution from the 0D void nucleation, 2D development, to 3D extension with related to the three typical stages of void accumulation of stable stage, transition stages, and failure stages. The growth type transition is attributed to the continuous void injection–leaded energy increase in the surficial Li atoms, which promotes the Li adatom diffusion–induced 3D extension. Variable current loading will lead to unpredictable interfacial morphological evolution, which can import difficulties in remaining the interfacial reversibility at practical application scenarios. According to the void formation theory, improving inherent void diffusivity, suppressing interfacial polarization, and constructing Li frameworks with porosity lower than the critical void size are potential principles to overcome the interfacial void–induced dilemmas, which can promote the wide applications of practical all-SSLMBs.

MATERIALS AND METHODS
Experimental section
Battery assembly
The batteries for performance evaluation are assembled with Li metal, Li$_7$P$_3$S$_{11}$ SSE, and indium foil. The batteries are assembled in mold cells. The thickness of lithium foil is 33 μm (~6.6 mA·hour cm^{-2}), and the counter-electrode In foil is 100 μm. After the complete discharge, the In will only form LiIn phase with the stable potential of 0.622 V versus Li/Li$^+$. To simplify the battery disassembly, copper foil is added upon the Li foil and In foil for the subsequent analyses.

Electrochemical measurement
The GEISs are evaluated by Solartron EnergyLab XM. The currents for galvanostatic measurements are ranging from 1 to 10 mA cm^{-2}. The measurement interval for impedance is 0.25 mA·hour cm^{-2} during each GEIS process. The measurement would be terminated automatically at the cutoff voltage of −2 V. The pressure applied on the battery mold is 5 MPa, and the evaluation temperature is 25°C (room temperature).

The measurement frequencies for EIS range from 1 MHz to 0.1 Hz, with an amplitude of 10 mV. The voltage cut for GEIS measurement is −2.0 V versus Li/Li$^+$, which is defined as the complete contact loss. Routine Li stripping is also measured in mold cells by the LAND2001A system. The DRT is realized using the MATLAB-GUI toolbox explored by Wan et al., (34).

Characterizations

The cross sections of the Li/SSE interface and the corresponding morphology captures, energy dispersive spectroscopy mapping, and TOF-SIMS evaluations are acquired from Tescan S9000 PFIB-SEM. Each area for PFIB treatment is 100 μm by 100 μm or 50 μm by 50 μm. The currents for PFIB are ranging from 50 to 5 nA until acquiring the polished interface. The TOF-SIMS measurement is also completed by the Tescan S9000 system under the atmosphere of $<8 \times 10^{-4}$ Pa with a current of 0.6 to 1 nA. The ionic source for PFIB and TOF-SIMS is the high-power Xe ion with a beam energy of 30 kV. An SEM-EBSD combination system with the Aztec acquisition software (Oxford Instruments) was used to analyze the structure, crystal orientation, and phase of routine Li foil.

The operando optical observation is conducted on the self-designed facility (fig. S21). The prepressed Li metal anode, $Li_7P_3S_{11}$ electrolyte, and In foil are sealed in these optical molds, and the images are captured using a Nikon SMZ25 optical microscope.

Computational method

First-principles calculations based on DFT were performed to reveal the interfacial effect on the activity of Li atoms using the Vienna ab initio Simulation Package (50). The projector augmented wave method was used to describe the ion-electron interactions (51). The Perdew-Burke-Ernzerhof version of the generalized gradient approximation was adopted for the exchange-correlation energy (52). A kinetic energy cutoff of 320 eV was used for the plane wave expansion of the valence electron wave functions. A dense Γ-centered Monkhorst-Pack k-point mesh with a sampling density of 0.03 Å^{-1}, 10^{-6} eV cell^{-1} in total energy, and 5×10^{-1} eV Å^{-1} in force were adopted for the convergence criterion during structural optimization. The site energy is defined as $E_{site} = E_{total} - E_{vacancy}$ to evaluate the activity of Li atoms, in which E_{total} and $E_{vacancy}$ are the total energy of a complete structure and a structure containing a vacancy, respectively.

SUPPLEMENTARY MATERIALS

Supplementary material for this article is available at https://science.org/doi/10.1126/sciadv.add0510

REFERENCES AND NOTES

1. L. Xu, Y. Lu, C.-Z. Zhao, H. Yuan, G.-L. Zhu, L.-P. Hou, Q. Zhang, J.-Q. Huang, Toward the scale-up of solid-state lithium metal batteries: The gaps between lab-level cells and practical large-format batteries. *Adv. Energy Mater.* **11**, 2002360 (2020).

2. A. Banerjee, X. Wang, C. Fang, E. A. Wu, Y. S. Meng, Interfaces and interphases in all-solid-state batteries with inorganic solid electrolytes. *Chem. Rev.* **120**, 6878–6933 (2020).

3. D. Cao, X. Sun, Q. Li, A. Natan, P. Xiang, H. Zhu, Lithium dendrite in all-solid-state batteries: Growth mechanisms, suppression strategies, and characterizations. *Matter* **3**, 57–94 (2020).

4. Y. Lu, C. Z. Zhao, H. Yuan, J. K. Hu, J. Q. Huang, Q. Zhang, Dry electrode technology, the rising star in solid-state battery industrialization. *Matter* **5**, 876–898 (2022).

5. X. B. Cheng, R. Zhang, C. Z. Zhao, Q. Zhang, Toward safe lithium metal anode in rechargeable batteries: A review. *Chem. Rev.* **117**, 10403–10473 (2017).

6. H. Liu, X.-B. Cheng, J.-Q. Huang, H. Yuan, Y. Lu, C. Yan, G.-L. Zhu, R. Xu, C.-Z. Zhao, L.-P. Hou, C. He, S. Kaskel, Q. Zhang, Controlling dendrite growth in solid-state electrolytes. *ACS Energy Lett.* , 833–843 (2020).

7. P. Wang, W. Qu, W.-L. Song, H. Chen, R. Chen, D. Fang, Electro–chemo–mechanical issues at the interfaces in solid-state lithium metal batteries. *Adv. Funct. Mater.* **29**, 1900950 (2019).

8. Y. Xiao, Y. Wang, S.-H. Bo, J. C. Kim, L. J. Miara, G. Ceder, Understanding interface stability in solid-state batteries. *Nat. Rev. Mater.* **5**, 105–126 (2019).

9. Y. Lu, C. Z. Zhao, H. Yuan, X. B. Cheng, J. Q. Huang, Q. Zhang, Critical current density in solid-state lithium metal batteries: Mechanism, influences, and strategies. *Adv. Funct. Mater.* **31**, 2009925 (2021).

10. T. Krauskopf, F. H. Richter, W. G. Zeier, J. Janek, Physicochemical concepts of the lithium metal anode in solid-state batteries. *Chem. Rev.* **120**, 7745–7794 (2020).

11. W. Frank, U. Breier, C. Elsasser, M. Fahnle, First-principles calculations of absolute concentrations and self-diffusion constants of vacancies in lithium. *Phys. Rev. Lett.* **77**, 518–521 (1996).

12. T. Krauskopf, B. Mogwitz, C. Rosenbach, W. G. Zeier, J. Janek, Diffusion limitation of lithium metal and Li–Mg Alloy anodes on LLZO type solid electrolytes as a function of temperature and pressure. *Adv. Energy Mater.* **9**, 1902568 (2019).

13. M. Jäckle, K. Helmbrecht, M. Smits, D. Stottmeister, A. Groß, Self-diffusion barriers: Possible descriptors for dendrite growth in batteries? *Energ. Environ. Sci.* **11**, 3400–3407 (2018).

14. T. Krauskopf, H. Hartmann, W. G. Zeier, J. Janek, Toward a fundamental understanding of the lithium metal anode in solid-state batteries—An electrochemo-mechanical study on the garnet-type solid electrolyte $Li_{6.25}Al_{0.25}La_3Zr_2O_{12}$. *ACS Appl. Mater. Interfaces* **11**, 14463–14477 (2019).

15. M. J. Wang, R. Choudhury, J. Sakamoto, Characterizing the Li-solid-electrolyte interface dynamics as a function of stack pressure and current density. *Joule* **3**, 2165–2178 (2019).

16. Y. Lu, C.-Z. Zhao, R. Zhang, H. Yuan, L.-P. Hou, Z.-H. Fu, X. Chen, J.-Q. Huang, Q. Zhang, The carrier transition from Li atoms to Li vacancies in solid-state lithium alloy anodes. *Sci. Adv.* **7**, eabi5520 (2021).

17. J. Kasemchainan, S. Zekoll, D. Spencer Jolly, Z. Ning, G. O. Hartley, J. Marrow, P. G. Bruce, Critical stripping current leads to dendrite formation on plating in lithium anode solid electrolyte cells. *Nat. Mater.* **18**, 1105–1111 (2019).

18. M. Wang, J. B. Wolfenstine, J. Sakamoto, Temperature dependent flux balance of the Li/$Li_7La_3Zr_2O_{12}$ interface. *Electrochim. Acta* **296**, 842–847 (2019).

19. Y. Lu, X. Huang, Z. Song, K. Rui, Q. Wang, S. Gu, J. Yang, T. Xiu, M. E. Badding, Z. Wen, Highly stable garnet solid electrolyte based Li–S battery with modified anodic and cathodic interfaces. *Energy Storage Mater.* **15**, 282–290 (2018).

20. F. N. Jiang, S. J. Yang, H. Liu, X. B. Cheng, L. Liu, R. Xiang, Q. Zhang, S. Kaskel, J. Q. Huang, Mechanism understanding for stripping electrochemistry of Li metal anode. *SusMat* **1**, 506–536 (2021).

21. C. Yang, H. Xie, W. Ping, K. Fu, B. Liu, J. Rao, J. Dai, C. Wang, G. Pastel, L. Hu, An electron/ion dual-conductive alloy framework for high-rate and high-capacity solid-state lithium-metal batteries. *Adv. Mater.* **31**, 1804815 (2019).

22. J. Tippens, J. C. Miers, A. Afshar, J. A. Lewis, F. J. Q. Cortes, H. Qiao, T. S. Marchese, C. V. di Leo, C. Saldana, M. T. McDowell, Visualizing chemomechanical degradation of a solid-state battery electrolyte. *ACS Energy Lett.* **4**, 1475–1483 (2019).

23. J. A. Lewis, F. J. Q. Cortes, Y. Liu, J. C. Miers, A. Verma, B. S. Vishnugopi, J. Tippens, D. Prakash, T. S. Marchese, S. Y. Han, C. Lee, P. P. Shetty, H. W. Lee, P. Shevchenko, F. de Carlo, C. Saldana, P. P. Mukherjee, M. T. McDowell, Linking void and interphase evolution to electrochemistry in solid-state batteries using operando x-ray tomography. *Nat. Mater.* **20**, 503–510 (2021).

24. D. Devaux, K. J. Harry, D. Y. Parkinson, R. Yuan, D. T. Hallinan, A. A. MacDowell, N. P. Balsara, Failure mode of lithium metal batteries with a block copolymer electrolyte analyzed by x-ray microtomography. *J. Electrochem. Soc.* **162**, A1301–A1309 (2015).

25. W. Chang, R. May, M. Wang, G. Thorsteinsson, J. Sakamoto, L. Marbella, D. Steingart, Evolving contact mechanics and microstructure formation dynamics of the lithium metal-$Li_7La_3Zr_2O_{12}$ interface. *Nat. Commun.* **12**, 6369 (2021).

26. M. B. Dixit, N. Singh, J. P. Horwath, P. D. Shevchenko, M. Jones, E. A. Stach, T. S. Arthur, K. B. Hatzell, In situ investigation of chemomechanical effects in thiophosphate solid electrolytes. *Matter* **3**, 2138–2159 (2020).

27. M. B. Dixit, A. Verma, W. Zaman, X. Zhong, P. Kenesei, J. S. Park, J. Almer, P. P. Mukherjee, K. B. Hatzell, Synchrotron imaging of pore formation in li metal solid-state batteries aided by machine learning. *ACS Appl. Energy Mater.* **3**, 9534–9542 (2020).

28. E. Kazyak, R. Garcia-Mendez, W. S. LePage, A. Sharafi, A. L. Davis, A. J. Sanchez, K. H. Chen, C. Haslam, J. Sakamoto, N. P. Dasgupta, Li penetration in ceramic solid electrolytes: Operando microscopy analysis of morphology, propagation, and reversibility. *Matter* **2**, 1025–1048 (2020).

29. H. Koshikawa, S. Matsuda, K. Kamiya, M. Miyayama, Y. Kubo, K. Uosaki, K. Hashimoto, S. Nakanishi, Dynamic changes in charge-transfer resistance at Li Metal/$Li_7La_3Zr_2O_{12}$ interfaces during electrochemical li dissolution/deposition cycles. *J. Power Sources* **376**, 147–151 (2018).

30. T. Krauskopf, R. Dippel, H. Hartmann, K. Peppler, B. Mogwitz, F. H. Richter, W. G. Zeier, J. Janek, Lithium-metal growth kinetics on LLZO garnet-type solid electrolytes. *Joule* **3**, 2030–2049 (2019).

31. I. D. Seymour, A. Aguadero, Suppressing void formation in all-solid-state batteries: The role of interfacial adhesion on alkali metal vacancy transport. *J. Mater. Chem. A* **9**, 19901–19913 (2021).

32. M. Yang, Y. Liu, A. M. Nolan, Y. Mo, Interfacial atomistic mechanisms of lithium metal stripping and plating in solid-state batteries. *Adv. Mater.* **33**, 2008081 (2021).

33. C.-T. Yang, Y. Qi, Maintaining a flat Li surface during the Li stripping process via interface design. *Chem. Mater.* **33**, 2814–2823 (2021).

34. T. H. Wan, M. Saccoccio, C. Chen, F. Ciucci, Influence of the discretization methods on the distribution of relaxation times deconvolution: Implementing radial basis functions with DRTtools. *Electrochim. Acta* **184**, 483–499 (2015).

35. Y. Lu, C.-Z. Zhao, J.-Q. Huang, Q. Zhang, The timescale identification decoupling complicated kinetic processes in lithium batteries. *Joule* **6**, 1172–1198 (2022).

36. F. M. Pesci, A. Bertei, R. H. Brugge, S. P. Emge, A. K. O. Hekselman, L. E. Marbella, C. P. Grey, A. Aguadero, Establishing ultralow activation energies for lithium transport in garnet electrolytes. *ACS Appl. Mater. Interfaces* **12**, 32806–32816 (2020).

37. R. D. Kelley, K. Song, B. Van Leer, D. Wall, L. Kwakman, Xe⁺ FIB milling and measurement of amorphous silicon damage. *Microsc. Microanal.* **19**, 862–863 (2013).

38. B. Van Leer, A. Genc, R. Passey, Ga⁺ and Xe⁺ FIB milling and measurement of Fib damage in aluminum. *Microsc. Microanal.* **23**, 296–297 (2017).

39. J. Z. Lee, T. A. Wynn, M. A. Schroeder, J. Alvarado, X. Wang, K. Xu, Y. S. Meng, Cryogenic focused ion beam characterization of lithium metal anodes. *ACS Energy Lett.* **4**, 489–493 (2019).

40. H. Yan, K. Tantratian, K. Ellwood, E. T. Harrison, M. Nichols, X. Cui, L. Chen, How does the creep stress regulate void formation at the lithium-solid electrolyte interface during stripping? *Adv. Energy Mater.* **12**, 2102283 (2021).

41. R. Raj, Nucleation of voids at Li-metal–ceramic–electrolyte interfaces. *MRS Commun.* **11**, 644–649 (2021).

42. A. Pei, G. Zheng, F. Shi, Y. Li, Y. Cui, Nanoscale nucleation and growth of electrodeposited lithium metal. *Nano Lett.* **17**, 1132–1139 (2017).

43. R. Raj, Stack pressure and critical current density in Li-metal cells: The role of mechanical deformation. *Acta Mater.* **215**, 117076 (2021).

44. R. Boistelle, J. P. Astier, Crystallization mechanisms in solution. *J. Cryst. Growth* **90**, 14–30 (1988).

45. Y. Chen, Z. Wang, X. Li, X. Yao, C. Wang, Y. Li, W. Xue, D. Yu, S. Y. Kim, F. Yang, A. Kushima, G. Zhang, H. Huang, N. Wu, Y. W. Mai, J. B. Goodenough, J. Li, Li metal deposition and stripping in a solid-state battery via coble creep. *Nature* **578**, 251–255 (2020).

46. J. M. Doux, H. Nguyen, D. H. S. Tan, A. Banerjee, X. Wang, E. A. Wu, C. Jo, H. Yang, Y. S. Meng, Stack pressure considerations for room-temperature all-solid-state lithium metal batteries. *Adv. Energy Mater.* **10**, 1903253 (2019).

47. Y. Lu, X. Huang, Y. Ruan, Q. Wang, R. Kun, J. Yang, Z. Wen, An in situ element permeation constructed high endurance Li–LLZO interface at high current densities. *J. Mater. Chem. A* **6**, 18853–18858 (2018).

48. A. Masias, N. Felten, R. Garcia-Mendez, J. Wolfenstine, J. Sakamoto, Elastic, plastic, and creep mechanical properties of lithium metal. *J. Mater. Sci.* **54**, 2585–2600 (2018).

49. X. Zhang, Q. J. Wang, K. L. Harrison, S. A. Roberts, S. J. Harris, Pressure-driven interface evolution in solid-state lithium metal batteries. *Cell Rep. Phys. Sci.* **1**, 100012 (2020).

50. G. Kresse, J. Furthmüller, Efficiency of ab-initio total energy calculations for metals and semiconductors using a plane-wave basis set. *Comput. Mater. Sci.* **6**, 15–50 (1996).

51. P. E. Blöchl, Projector augmented-wave method. *Phys. Rev. B* **50**, 17953–17979 (1994).

52. J. P. Perdew, K. Burke, M. Ernzerhof, Generalized gradient approximation made simple. *Phys. Rev. Lett.* **77**, 3865–3868 (1996).